A long-time-step-permitting tracer transport model on the regular latitude-longitude grid

Jianghao LI[1,3], and Li DONG*[2,4]

[1]*Key Laboratory of Earth System Modeling and Prediction, China Meteorological Administration, Beijing* 100081*, China*

[2]*State key Laboratory of Numerical Modeling for Atmospheric Sciences and Geophysical Fluid Dynamics (LASG), Institute of Atmospheric Physics (IAP), Chinese Academy of Sciences, Beijing* 100029, *China*

[3]*State Key Laboratory of Severe Weather (LaSW), Chinese Academy of Meteorological Sciences, China Meteorological Administration, Beijing* 100081*, China*

[4]*College of Earth and Planetary Sciences, University of Chinese Academy of Sciences, Beijing, China*

ABSTRACT

If an explicit time scheme is used in a numerical model, the size of the integration time step is typically limited by the spatial resolution. This study develops a regular latitude–longitude grid-based global three-dimensional tracer transport model that is computationally stable at large time-step sizes. The tracer model employs a finite-volume flux-form semi-Lagrangian (FFSL) transport scheme in the horizontal and an

*Corresponding author: Li DONG
Email: dongli@lasg.iap.ac.cn

adaptively implicit algorithm in the vertical. The horizontal and vertical solvers are coupled via a straightforward operator-splitting technique. Both the finite-volume scheme's one-dimensional slope-limiter and the adaptively implicit vertical solver's first-order upwind scheme enforce monotonicity. The tracer model permits a large time-step size and is inherently conservative and monotonic. Idealized advection test cases demonstrate that the three-dimensional transport model performs very well in terms of accuracy, stability, and efficiency. It is possible to use this robust transport model in a global atmospheric dynamical core.

Key words: tracer transport, numerical stability, latitude-longitude grid

https://doi.org/10.1007/s00376-023-2270-z

Article Highlights:

- A three-dimensional tracer transport model is developed on a regular latitude–longitude grid wherein the time-step size is unlimited by the horizontal resolution to a large extent.
- The adaptively implicit vertical advection scheme improves the numerical stability of the vertical advection process.
- The tracer transport model preserves the positive definiteness or monotonicity without explicit diffusion.

1. Introduction

To improve the forecast or simulation skill, global weather and climate models generally resolve more atmospheric motions by increasing their spatial resolutions, such as in global storm-resolving or cloud-resolving models (e.g., Stevens et al., 2019;

Satoh et al., 2019). Moreover, most weather and climate models use higher resolutions in the vertical than in the horizontal. As the horizontal and vertical spatial resolution increases, the advective Courant number (or Courant–Friedrichs–Lewy, CFL) becomes the primary factor that constrains the model time-step if an explicit time scheme is applied. The Courant number should be less than a specific scheme-dependent constant (typically, unity); otherwise, the model would be numerically unstable. This Courant number limitation is even more strict for global models with a latitude–longitude grid because of the convergence of the meridians at the poles (Lin and Rood, 1996; Weller et al., 2022).

For atmospheric models that use the latitude–longitude grid, there are a few alleviations to the Courant number limitation. Semi-Lagrangian time-stepping techniques, which are widely used in atmospheric models, allow for larger time-step sizes than the CFL-constrained Eulerian methods do (Wood et al., 2014); however, the classical semi-Lagrangian transport scheme does not formally conserve the total mass (Staniforth and Côté, 1991; Diamantakis, 2014). The lack of mass conservation for certain quantities is inadequate for long-term simulations and for the overall accuracy of atmospheric models.

Another approach to removing the Courant number restriction is using implicit advection schemes. The virtue of implicit methods is the attractive unconditional stability properties, thus allowing large Courant numbers in terms of stability (Hundsdorfer and Verwer, 2003). However, one disadvantage of implicit time-stepping methods is the computational cost of solving a matrix equation. Other disadvantages of implicit advection schemes include large phase errors when using large time-step sizes and difficulties in achieving monotonicity (Chen et al., 2017).

An alternative straightforward approach to alleviating the CFL constraint on a latitude–longitude grid is the application of a quasi-uniform spherical grid (Williamson, 2007; Staniforth and Thuburn, 2012). For instance, the pole problem on a latitude–longitude grid is almost completely avoided by using a cubed-sphere or icosahedral grid. A quasi-uniform spherical grid, however, lacks the latitudinal regularity of the rotational Earth. Additionally, the internal boundary or singularity of the polygon needs to be specifically addressed, which could lead to computational mode and grid imprinting (Weller, 2012).

There are also several desired properties of numerical schemes for tracer transport, such as monotonicity, shape preservation, positivity, and mass conservation (refer to Lauritzen et al., 2011 for a comprehensive review). Flux-corrected transport (FCT) is a monotonicity-preserving method that computes and limits flux using both a low-order monotonic method and a higher-order scheme (e.g., Book et al., 1981; Boris and Book, 1997; Zalesak, 1979). The slope-limiter method (LeVeque, 2004; Durran, 2010) is another approach that estimates the flux at the cell interface by fitting a piecewise parabola to a finite-volume average of the transported scalar field. These parabolas are subsequently modified to ensure monotonicity is preserved. This study uses both methods to obtain monotonicity.

We have developed a new shallow-water model of the Grid-point Atmospheric Model of IAP (Institute of Atmospheric Physics) LASG (State key Laboratory of

Numerical Modeling for Atmospheric Sciences and Geophysical Fluid Dynamics) (Li et al., 2020), and a baroclinic dynamical core on the latitude–longitude grid is also being developed. The tracer transport module is a crucial component of any weather or climate model. This study takes a further step towards creating a full model by designing a global atmospheric tracer transport model on a regular latitude–longitude grid. First, the FFSL tracer transport algorithm developed by Lin and Rood (1996) is employed horizontally. The semi-Lagrangian property of the FFSL guarantees computational stability when the zonal Courant number is greater than unity, reducing the restrictive limitations on the polar regions. Second, an adaptively implicit vertical transport scheme (Shchepetkin, 2015; Wicker and Skamarock, 2020; Li and Zhang, 2022) is adopted to alleviate the vertical stability limitations. The time-step size in the tracer model will be significantly improved by combining these two approaches. This study presents the computational scheme of the three-dimensional transport model, along with the accuracy, stability, and monotonicity of the model.

The remainder of this manuscript is organized as follows. Section 2 describes the horizontal and vertical transport solvers in detail. Section 3 presents results from several well-known idealized 2D and 3D test cases, and a brief conclusion is provided in section 4.

2. Horizontal and vertical solvers

We define the horizontal and vertical grid structures used in this study before introducing the solvers in detail. A regular latitude–longitude grid is used in the horizontal discretization, where winds and tracers are staggered with the Arakawa C-grid (Arakawa and Lamb, 1977). The wind component is defined at the middle of the cell interface, while the tracer concentration is defined at the cell center and the Earth's poles. We use a stationary, non-uniform, mass-based, and terrain-following vertical coordinate (Kasahara, 1974; Simmons and Burridge, 1981; Laprise, 1992), with the positive direction pointing downward, and top-down numbering. A Lorenz-type staggering is adopted in the vertical, which means that the vertical coordinate velocity and vertical mass flux are defined at half levels, and the tracer mass-mixing ratio is defined at full levels.

With a general vertical coordinate η, the tracer conservation equation without sources or sinks can be written as:

$$\frac{\partial}{\partial t}\left(\frac{\partial \pi}{\partial \eta} q\right) + \nabla_\eta \cdot \left(\frac{\partial \pi}{\partial \eta}\mathbf{V}_h q\right) + \frac{\partial}{\partial \eta}\left(\frac{\partial \pi}{\partial \eta}\dot{\eta} q\right) = 0, \quad (1)$$

where π is the hydrostatic pressure (Laprise, 1992), $\frac{\partial \pi}{\partial \eta}$ is the pseudo-density, and q is the tracer mixing ratio. $\nabla_\eta \cdot ()$ represents the horizontal divergence operator, which can be discretized based on the Gauss theorem. $\mathbf{V}_h$ is the two-dimensional horizontal velocity vector, and $\dot{\eta}$ is the vertical coordinate velocity. For the purpose of spatial discretization, the layer-averaged formulation (eq. 12 in Zhang et al., 2020) is used in this study. $\mathbf{V}_h$ and q represent layer-averaged states; consequently, the tracer equation can be further expressed as:

$$\frac{\partial(\delta\pi q)}{\partial t} + \nabla_\eta \cdot (\delta\pi \mathbf{V}_h q) + \delta\left(\frac{\partial \pi}{\partial \eta}\dot{\eta} q\right) = 0, \quad (2)$$

where $\delta\pi$ denotes the layer mass in a full level, $\delta\pi_k = \pi_{k+1/2} - \pi_{k-1/2}$. The δ operator in the third term denotes the difference between two half levels, which is defined at the full levels: $\delta\left(\frac{\partial \pi}{\partial \eta}\dot{\eta} q\right)_k = \left(\frac{\partial \pi}{\partial \eta}\dot{\eta} q\right)_{k+1/2} - \left(\frac{\partial \pi}{\partial \eta}\dot{\eta} q\right)_{k-1/2}$.

To implement the adaptively implicit vertical transport scheme, the mass-weighted vertical velocity $\left(\frac{\partial\pi}{\partial\eta}\dot{\eta}\right)$ is split into explicit and implicit velocities for the explicit and implicit transport parts, respectively. Thus, the equation can be semi-discretized as:

$$\frac{\partial(\delta\pi q)}{\partial t} + \nabla_\eta \cdot (\delta\pi \mathbf{V}_h q) + \delta\left[\left(\frac{\partial\pi}{\partial\eta}\dot{\eta}\right)_E q\right] + \delta\left[\left(\frac{\partial\pi}{\partial\eta}\dot{\eta}\right)_I q\right] = 0, \tag{3}$$

where the explicit and implicit vertical velocities are partitioned from the full vertical velocity:

$$\left(\frac{\partial\pi}{\partial\eta}\dot{\eta}\right)_E = \beta\left(\frac{\partial\pi}{\partial\eta}\dot{\eta}\right), \tag{4}$$

$$\left(\frac{\partial\pi}{\partial\eta}\dot{\eta}\right)_I = (1-\beta)\left(\frac{\partial\pi}{\partial\eta}\dot{\eta}\right), \tag{5}$$

where the splitting parameter β is a transition function responsible for the splitting of the vertical velocity between a fully explicit solver ($\beta = 1$) and a fully implicit solver ($\beta = 0$), which is determined by the local Courant number. We do not describe the calculating formulation of β and related parameters since these can be found in Wicker and Skamarock (2020). This approach has the advantage of rendering vertical advection stable and maintaining high accuracy in locations with low Courant numbers.

The fractional step, also known as operator-splitting, is attractive for solving the three-dimensional equation because of its efficiency and high accuracy in each spatial dimension (e.g., LeVeque, 2004; Lin and Rood, 1996; Putman and Lin, 2007). The operator-splitting is applied between horizontal and vertical operators to make it simpler to implement an implicit integration scheme in the vertical, although the operator-splitting is first-order accurate in time. A form of Strang splitting (Strang, 1968) can also be used to achieve second-order accuracy. After calculating the horizontal operator, the updated tracer mass-mixing ratio is used for the vertical operator.

The computational procedures are as follows:

(i) Calculate the horizontal flux for the intermediate variable using

$$(\delta\pi q)^* = (\delta\pi q)^n - \Delta t \nabla_\eta \cdot \left[(\delta\pi q)^n \mathbf{V}_h\right]. \tag{6}$$

In our model, the Lin and Rood (1996) FFSL approach is used, which is based on forward Euler explicit time differencing (a two time-level scheme). The essence of the FFSL method is that the 2D flux divergence is split into two orthogonal 1D flux-form transport operators. The flux is approximately equal to the air-mass flux times the tracer mixing ratio on the cell interface in a one-dimensional direction. Either the piecewise linear van Leer method or the Piecewise Parabolic Method (PPM, Colella and Woodward, 1984; Carpenter et al., 1990) can be used to reconstruct the tracer in a mesh cell by using mean values of surrounding cells. We choose the PPM for our model because of its accuracy and computational efficiency. In addition, a monotonicity constraint (or slope-limiter) can be imposed on the 1D discrete solution, but, due to dimensional splitting, this does not ensure exact monotonicity in the overall 2D solution (Lin and Rood, 1996; Kent et al., 2012). The slope-limiter would damp the numerical oscillations but introduce diffusion in the numerical solutions. We used the modified version of the PPM limiter from Appendix B of Lin (2004) for both the horizontal and vertical advections. A minor correction regarding the limiter is noted in the appendix of this manuscript.

A semi-Lagrangian approach is also used in the longitudinal (east–west) direction on the latitude–longitude grid to alleviate the pole problem. The flux across cell interfaces is calculated by integrating the swept volume over a large number of upstream zonal cells. This approach enlarges the upwind-biased computation stencil that relaxes the CFL linear stability constraint, especially near the poles, as stated in section 3 of Lin and Rood (1996). Since the method is in the flux-form (The FF abbreviation in FFSL), it guarantees the total tracer mass conservation, whereas the conventional method that tracks point does not make this guarantee. The pure Eulerian counterpart is used in the meridional (north–south) direction, so the time-step size is only constrained by the meridional Courant number.

For comparison, we also implement a third-order upwind flux formulation combined with a third-order Runge–Kutta (RK3) time integrator (Wicker and Skamarock, 2002, hereafter RK3O3) in the horizontal solver. Unlike FFSL, RK3O3 is a method of lines (MOL, Hyman,1979; Shchepetkin, 2015), where the spatial and temporal discretizations are decoupled and treated separately. The FCT algorithm (Zalesak, 1979) is applied in the RK3O3 to restore positive definiteness or monotonicity. It should be noted that the FCT operator can be applied either on each sub-step or the last sub-step of the RK3 scheme. In our tests, the former guarantees strict monotonicity, while the latter cannot (see section 3.1).

(ii) Update the mass-weighted mixing ratio in the vertical explicit residual with:

$$(\delta\pi q)^{**} = (\delta\pi q)^{*} - \Delta t\delta\left[\left(\frac{\partial\pi}{\partial\eta}\dot{\eta}\right)_E q^{*}\right], \tag{7}$$

where $q^{*} = \frac{(\delta\pi q)^{*}}{\delta\pi^{n+1}}$, and the layer mass $\delta\pi^{n+1}$ can be obtained by the continuity equation in the dynamical core of a full model. The layer mass is unchanged with time in the passive tracer advection tests. The explicit vertical velocity $\left(\frac{\partial\pi}{\partial\eta}\dot{\eta}\right)_E$ is used in the

1D finite-volume scheme. As in the horizontal solver, we can obtain the vertical flux at half levels by using the third-order upwind flux operator or the PPM finite-volume method. The third-order upwind flux operator combines with the RK3 time-integrator method (RK3O3), whereas the PPM flux operator is equipped with the forward Eulerian time integration. Similarly, the FCT and slope-limiter can be imposed on the RK3O3 and PPM flux operators, respectively. The performance of these schemes will be evaluated by the following test cases.

(iii) At the last step, update the tracer using an implicit algorithm with:

$$(\delta\pi q)^{n+1} = (\delta\pi q)^{**} - \Delta t\delta\left[\left(\frac{\partial\pi}{\partial\eta}\dot{\eta}\right)_I q^{n+1}\right]. \tag{8}$$

Because it is the only inherently monotonic linear scheme (Godunov, 1959), the first-order upwind scheme is chosen to calculate the vertical mass flux at the half interface. While other higher-order nonlinear schemes are theoretically possible, the first-order upwind method is typically more cost-effective. Then mixing ratio at a new time level can be obtained by $q^{n+1} = \frac{(\delta\pi q)^{n+1}}{\delta\pi^{n+1}}$. Since each unknown q_k^{n+1} depends on its upper q_{k-1}^{n+1} and lower q_{k+1}^{n+1} neighbors (subscript k is used for the variable located in the full layer in the vertical direction), the above set of equations form a tridiagonal system in a vertical column. The system of linear equations can be solved with a tridiagonal matrix algorithm (TDMA).

The summary of flux operators and monotonic limiters used in the model for the idealized tests is provided in Table 1.

Table 1. List of the horizontal and vertical flux operators, along with the corresponding limiters in the tracer transport model.

The horizontal flux	The vertical explicit flux	The vertical implicit flux

operator/limiter	operator/limiter	operator
FFSL/slope-limiter	PPM/slope-limiter	1^{st}-order upwind
RK3O3/FCT	RK3O3/FCT	

3. Transport tests

This section discusses the results of the transport model runs using four standard passive-tracer transport test cases. The test cases have varying degrees of complexity in two and three dimensions. All the test cases use a prescribed time-(in)dependent flow field. The accuracy and properties of the two-dimensional transport scheme are evaluated using two-dimensional horizontal tests. Two additional three-dimensional passive-tracer transport test cases from Kent et al. (2014) are performed in our model. They are used to demonstrate the accuracy of horizontal–vertical coupling and the viability of the adaptively implicit vertical transport algorithm.

Error norms can be calculated because the final tracer distribution for each test is ideally equal to the initial condition or is given analytically. The error norms of ℓ_1, ℓ_2, ℓ_∞ are defined as in Williamson et al. (1992):

$$\ell_1 = \frac{I[|q - q_T|]}{I[|q_T|]}, \tag{9}$$

$$\ell_2 = \left[\frac{I[(q - q_T)^2]}{I[(q_T)^2]}\right]^{\frac{1}{2}}, \tag{10}$$

$$\ell_\infty = \frac{\max\forall\, |q - q_T|}{\max\forall |q_T|}, \tag{11}$$

where q denotes the computational solution, q_T denotes the analytic or reference solution, $\max\forall$ selects the maximum value from a given field, and I is the global two-dimensional integral:

$$I(q)=\frac{1}{4\pi}\int_{0}^{2\pi}\int_{-\pi/2}^{\pi/2}q(\lambda,\varphi)\cos\varphi d\varphi d\lambda, \quad (12)$$

or the global three-dimensional integral:

$$I\ \ (q)\ \ =\frac{1}{4\pi(\eta_s-\eta_{top})}\int_{\eta_{top}}^{\eta_s}\int_{0}^{2\pi}\int_{-\pi/2}^{\pi/2}q(\lambda,\varphi,\eta)\cos\varphi d\varphi\ d\lambda\ d\eta. \quad (13)$$

3.1 Two-dimensional solid-body rotation test

The test case of solid-body rotation over the sphere (Williamson et al., 1992; test case 1) is widely used to assess 2D advection schemes. The nondivergent zonal and meridional velocities are given by:

$$u(\lambda,\varphi)=u_0(\cos\alpha\cos\varphi+\sin\alpha\cos\lambda\sin\varphi), \quad (14)$$

$$v(\lambda,\varphi)=-u_0\sin\alpha\sin\lambda, \quad (15)$$

where λ and φ are longitude and latitude, respectively. The maximum wind speed $u_0=\frac{2\pi a}{12\ \mathrm{days}}\approx 38.61\ \mathrm{m\ s^{-1}}$, and a is the radius of the Earth. α denotes the flow orientation angle to the equator, $\alpha=90^{\circ}$ corresponds to the advection of the solid body crossing the pole. Ideally, the solid body translates without changing shape and returns to its initial position after one rotation (12 days). We evaluate the horizontal advection solver from different aspects using three initial distributions.

First, to evaluate the positive definitiveness or monotonicity of the advection algorithm with limiters, the initial shape is set as two-slotted cylinders. The two-slotted cylinders centered on $(\lambda_0,\varphi_0)=(3\pi/2,0)$ are defined as:

$$q(\lambda,\varphi)=\begin{cases}1 & r_1\le r_0 \text{ and } \left(\varphi-\varphi_1<-\frac{5r_0}{12a} \text{ or } |\lambda-\lambda_1|>\frac{r_0}{6a}\right)\\ 1 & r_2\le r_0 \text{ and } \left(\varphi-\varphi_2>\frac{5r_0}{12a} \text{ or } |\lambda-\lambda_2|>\frac{r_0}{6a}\right)\\ 0.1 & \text{otherwise}\end{cases}, \quad (16)$$

where $(\lambda_1,\varphi_1)=(\lambda_0-\pi/6,\varphi_0)$, $(\lambda_2,\varphi_2)=(\lambda_0+\pi/6,\varphi_0)$, $r_0=a/2$, and r_1 and r_2

are the great circle distances:

$$r = a\arccos\left(\sin\varphi_c \sin\varphi + \cos\varphi_c \cos\varphi \cos\left(\lambda - \lambda_c\right)\right) \tag{17}$$

from (λ_1,φ_1) and (λ_2,φ_2), respectively.

Fig. 1 and Fig. 2 show the results of this test case using the RK3O3 and FFSL schemes with and without the monotonic limiters. The spatial resolutions are 2°, 1°, and 0.5°, and, when $\alpha = 90^\circ$, the maximum time-step sizes of the RK3O3 scheme are 288 s, 72 s, and 18 s. This guarantees that the Courant number is approximately constant (~1.43) at the three resolutions. The same time-step sizes as RK3O3 are applied to FFSL for comparison, although FFSL can take larger time-step sizes. Both schemes cannot prevent nonphysical under- and over-shoots in the absence of limiters, as evidenced by the values less than 0.1 or greater than 1. Since RK3O3 itself possesses some degree of dissipation (Wicker and Skamarock, 2002; Skamarock and Gassmann, 2011), the under- and over-shoots are slightly smaller in magnitude than the results of the FFSL scheme. The monotonic limiter would effectively eliminate the undershoots and overshoots, as shown in Fig. 2. In our model, it should be noted that the FCT flux limiter was activated during each RK3 time-integrator sub-step. If the FCT limiter is only applied on the last RK3 sub-step, undershoots and overshoots will still exist (not shown).

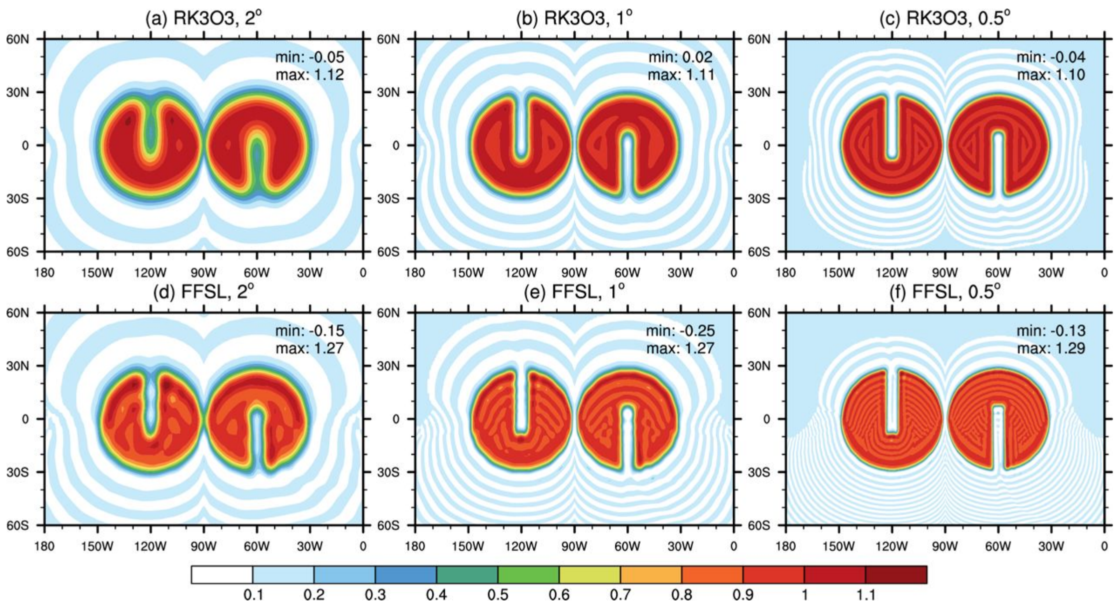

Fig. 1. Solid-body rotation of two-slotted cylinders with $\alpha = 90^{\circ}$ for spatial resolutions of 2°(left column), 1°(center column), and 0.5°(right column) using RK3O3 (upper row) and FFSL (bottom row) schemes without limiters at day 12. The minimum (min) and maximum (max) of the simulations are shown in each panel.

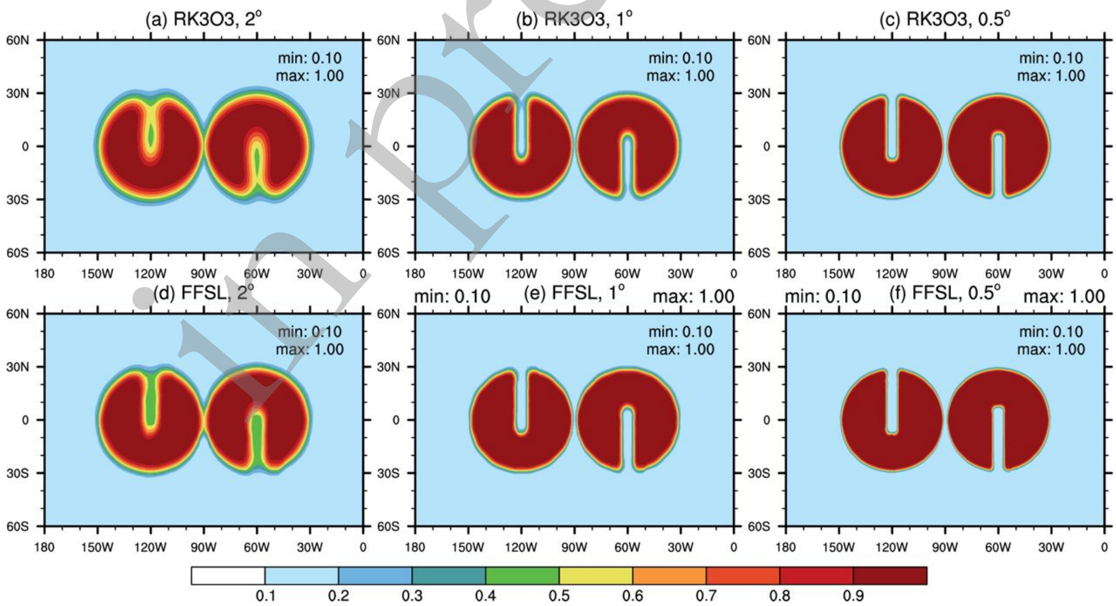

Fig. 2. Same as Fig.1, but the FCT limiter is applied at each sub-step of the RK3 time integrator, and the monotonic slope-limiter is used for the FFSL scheme.

Next, we evaluate the model simulating the solid body passing over the pole. The initial cosine-bell tracer distribution is:

$$q = \begin{cases} \frac{h_0}{2}\left[1 + \cos\left(\frac{\pi r}{R}\right)\right] & \text{if } r < R \\ 0 & \text{if } r \geq R \end{cases}, \tag{18}$$

where the radius $R = a/3$ and the maximum $h_0 = 1000$; r denotes the great circle distance between a position (λ,φ) and the center of the cosine bell $(\lambda_c,\varphi_c) = (3\pi/2, 0)$.

Fig. 3 presents the transport of the cosine bell structure over the North Pole using the RK3O3 and FFSL schemes with their respective FCT flux- and slope-limiters. The spatial resolution is 1°. First, set the time-step size to 72 s, which corresponds to the longitudinal and meridional Courant numbers of ~1.43 and ~0.025, respectively. When using much larger time-step sizes, the model with the RK3O3 scheme tends to become unstable. In other words, the RK3O3 permits a maximum Courant number of approximately 1.43 for stability. As shown in Fig. 3ab, neither scheme exhibits significant distortions. Using the FFSL scheme, the shape of the cosine bell undergoes stretching in the flow direction, which is typically observed in monotonic finite-volume advection algorithms (e.g., Lin and Rood, 1996; Nair and Machenhauer, 2002; Jablonowski et al., 2006).

In practice, the FFSL scheme allows for much longer time-step sizes. We increase the time-step size to 1440 s so that the zonal and meridional Courant numbers are ~28.64 and ~0.5, respectively, as shown in Fig. 3c. When passing over the North Pole, the cosine bell deforms slightly; if larger time-step sizes were used, the deformation would be more pronounced. However, no deformation was observed when the rotation angle was 0° or 45° (not shown). Therefore, the deformation possibly results from the large curvature of the Earth near the pole. Within the FFSL scheme, the departure point is only calculated in the zonal direction. In general, the larger the time-step size, the larger the halo width for parallel distributed-memory communication, which has an additional negative effect on the computational efficiency. Specialized parallel optimization could be conducted to mitigate this overhead, such as limiting the large halo within the polar region and using asynchronous communication, but it is beyond the scope of this work. Nevertheless, it is still worth pointing out that the FFSL scheme permits a much larger time-step size than the RK3O3 scheme does.

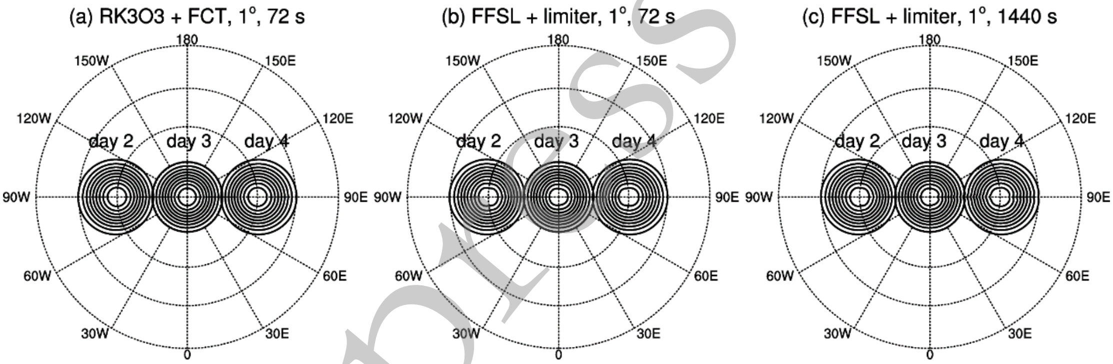

Fig. 3. Snapshots of the cosine bell passing over the North Pole (the outer circle is located at 30°N) at a resolution of 1° with the RK3O3 (a) and FFSL (b-c) schemes. The contour intervals are 100 m, and the zero contour is omitted. The time-step sizes used in the test are also shown in the title of each panel.

To further evaluate the accuracy of the two advection schemes, the advection of a Gaussian hill was

$$q(\lambda,\varphi) = \exp\left\{ -b_0\left[(X-X_c)^2 + (Y-Y_c)^2 + (Z-Z_c)^2\right]\right\}, \quad (19)$$

where $b_0 = 5$ defines the width of the Gaussian hill. (X, Y, Z) are the 3D absolute Cartesian coordinates corresponding to the spherical (λ,φ) coordinates:

$$(X,Y,Z) = (\cos\varphi\cos\lambda, \cos\varphi\sin\lambda, \sin\varphi). \tag{20}$$

The center of the Gaussian hill (X_c, Y_c, Z_c) is calculated by substituting $(3\pi/2, 0)$ for (λ, φ) in Eq. (20). This tracer distribution function is continuously differentiable, so the theoretical accuracy order of the horizontal solver can be estimated from the convergence rate of the error norms (e.g., Nair and Lauritzen, 2011; Skamarock and Gassmann, 2011; Kent et al., 2012).

Unlike in Kent et al. (2012), where the spatial resolution is variable and the time-step size is constant, in this case we continuously change the time-step size to hold the maximum zonal Courant number fixed. For $\alpha = 0^\circ$, the solid body is advected around the equator. The spatial resolutions range from 2° to 0.5°, and the corresponding time-step sizes are 2880 s, 1440 s, and 720 s. A constant Courant number of ~0.5 results from this configuration. For $\alpha = 45^\circ$, the time-step sizes are 480 s, 120 s, and 30 s, which result in a maximum Courant number of ~1.7. For $\alpha = 90^\circ$, the Gaussian bell is advected across the poles with time-step sizes of 288 s, 72 s, and 18 s, which give a constant Courant number of ~1.43.

The convergence plots for ℓ_2 and ℓ_∞ for the unlimited and limited variations of the RK3O3 and FI

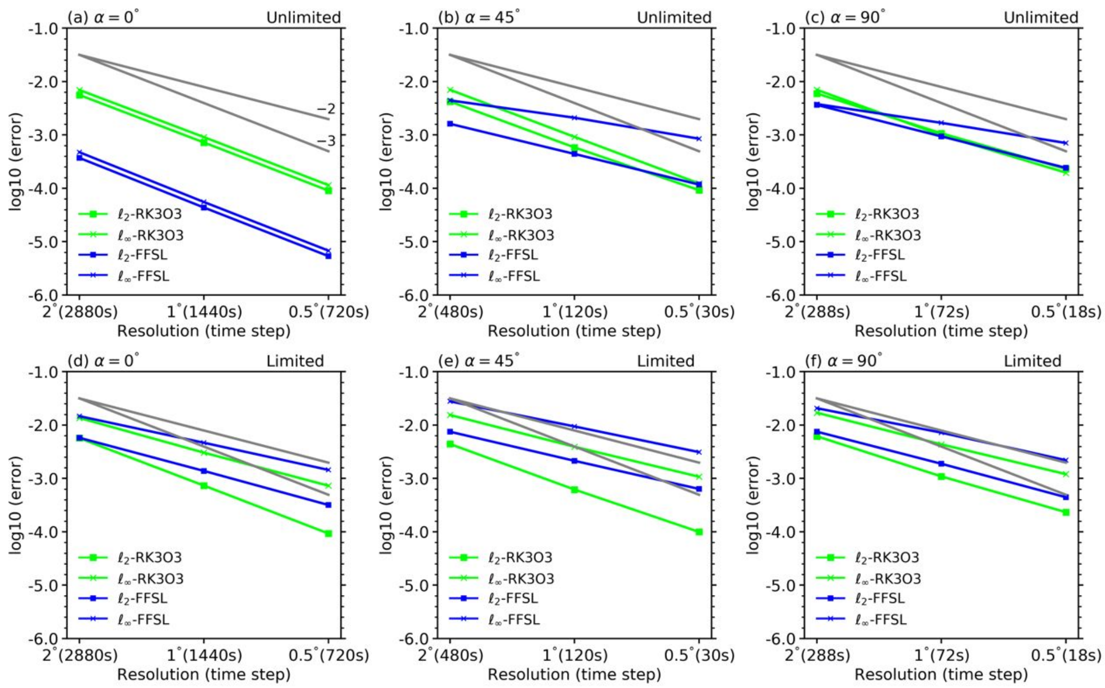

Fig. 4. Numerical convergence rates of ℓ_2 and ℓ_∞ for the unlimited (upper row) and limited (bottom row) variations of the RK3O3 and FFSL schemes in the Gaussian hill rotation test case for different rotational angles ($\alpha = 0°, 45°, 90°$). The second- and third-order convergence rates (top and bottom, respectively) are plotted as gray lines on each plot.

3.2 Two-dimensional moving vortices

This test combines the previous solid rotation flow with a deformational (nondivergent) vortex flow. Although the deformational flow field varies in time and space, analytical solutions are readily available. The deformational flow creates two vortices on the polar opposite sides of a rotating sphere. The vortices are transported at an angle α to the east of the equator in a background solid-body rotation. Here, the rotation angle is 90°, which corresponds to the cross-polar flow. Other parameters for this test case follow Nair and Jablonowski (2008) and Norman and Nair (2018). The initial positions of the two vortices are $(3\pi/2, 0)$ and $(\pi/2, 0)$. It takes 12 days for the two vortices to complete one rotation over the poles.

Fig. 5a and Fig. 5c present the numerical solution after 12 days of simulating the tracer field using the RK3O3 and FFSL schemes. To guarantee monotonicity, both the FCT flux limiter and slope-limiter are used. There is no significant difference between the two results. Fig. 5b and Fig. 5d give plots of the final solution and the exact solution along the equator, showing that the two schemes yield nearly identical solutions and diffusions due to the use of limiters. The phase error of FFSL is slightly smaller than that of RK3O3.

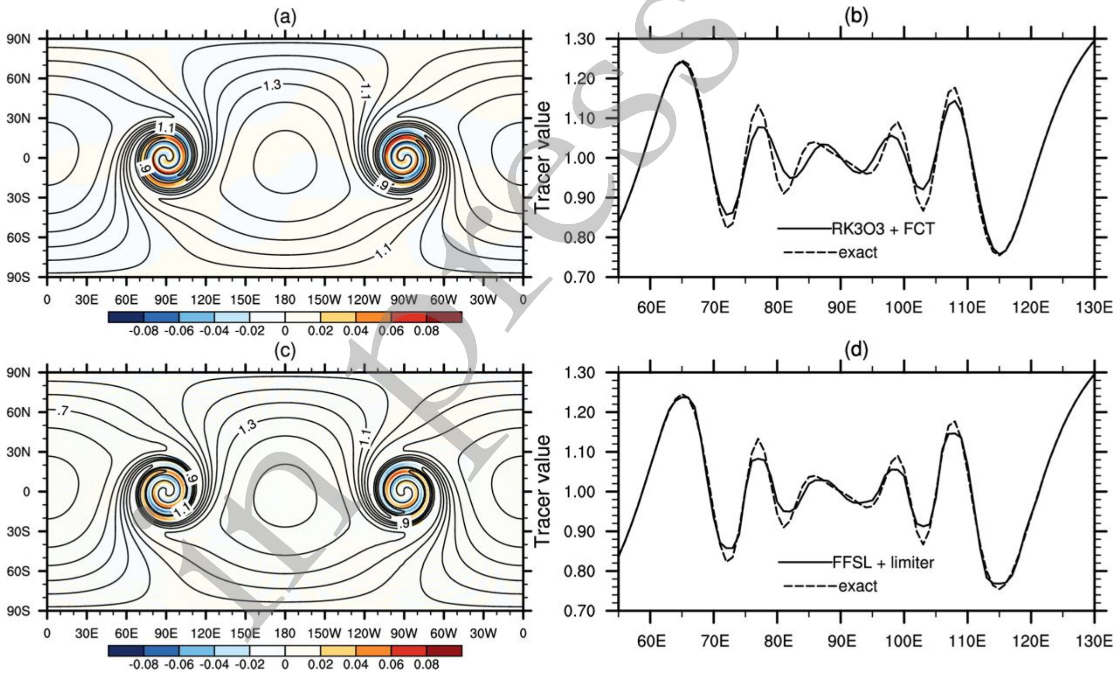

Fig. 5. Contour plots (a, c) of the moving vortices at day 12 computed with the limited variations of (a, b) RK3O3 and (c, d) FFSL. The contours in (a, c) are the computational solutions, and the shaded color indicates the difference between the computational and analytical solutions. (b) and (d) show the final solutions along the equator. The spatial resolution is 1°, and the time-step size is 90 s.

The convergence rates for this test case are shown in Fig. 6a. The two schemes' convergence rates are less than second order from 2° to 1° and approximately second order from 1° to 0.5°. The difference in the absolute errors between the two schemes is negligible. The present performance agrees with the previous simulations. However, the advantage of the FFSL scheme over the RK3O3 scheme is that it allows for a much larger time-step size. The sensitivity of the FFSL to the time-step size is displayed in Fig. 6b. We conduct experiments with time-step sizes of 20 s, 40 s, 80 s, and 160 s and a fixed horizontal resolution of 0.5°. A larger time-step size does not significantly affect the error norms, which is another advantageous feature of FFSL.

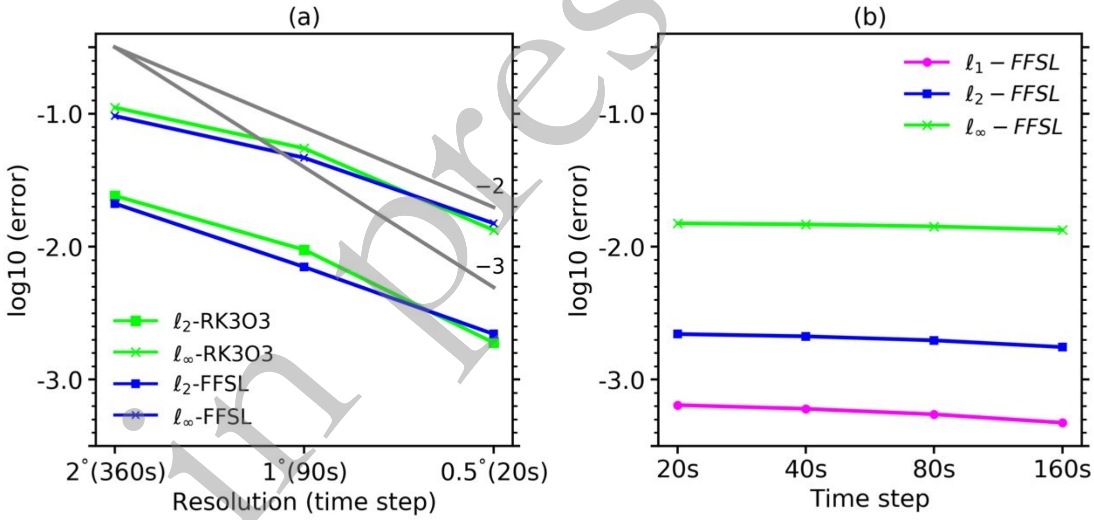

Fig. 6. Error norms in the test case of the two-dimensional moving vortex. The left panel shows the convergence rates of ℓ_2 and ℓ_∞ for the limited variations of the RK3O3 and FFSL schemes. The error norms of the FFSL with a fixed resolution of 0.5° and variable time-step sizes are displayed in the right panel.

3.3 Three-dimensional deformational flow

The test cases presented in the previous two subsections demonstrate the FFSL's accuracy and its capacity for increasing time-step size horizontally by contrasting it with the results of RK3O3. The vertical advection scheme, however, also influences the overall accuracy and stability of the real three-dimensional advection process. Furthermore, atmospheric tracers are often observed to have functional relationships in the real world; thus, transport schemes, such as those used in chemistry models, should not disrupt those functional relationships.

Here, we assess the advection scheme's ability to maintain the functional relationships using the three-dimensional deformational flow test (test 1-1, described in Kent et al., 2014). The prescribed wind velocities and tracer mixing ratios are described in Kent et al. (2014) and Hall et al. (2016). The 3D winds stretch the tracers (the nonlinearly correlated q_1 and q_2, both of which have spherical initial shapes, and q_3, which has an initial shape of two-slotted ellipses) over the first six days. When the tracers return to their original shapes and positions after being reversed by the flow, it is possible to calculate the error norms. On day 6, the tracer field has the most deformation.

The horizontal spatial resolution is 1°, with 60 uniformly spaced vertical levels in the height coordinate, as recommended in the Dynamical Core Model Intercomparison Project (DCMIP) test document. Specifically, we use a time-step size of 600 s and maximum Courant numbers of approximately 0.44, 0.17, and 0.02 in the longitudinal, meridional, and vertical directions, respectively. The adaptively implicit vertical advection algorithm is not activated because the wind speed is much weaker in the vertical direction (small Courant number). As a result, the simulation results of the adaptively implicit algorithm are the same as those of the fully explicit algorithm, which is expected and verified in this test.

We first assess the performance of different flux operators used by the horizontal and vertical solvers in the 3D transport model. On day 6, when the tracers stretch to their maximum, Fig. 7 presents the horizontal cross-sections of the tracer q_3 fields at a height of 4.9 km via four combinations of two horizontal flux operators and two vertical flux operators. Fig. 8 gives the results on day 12 when the tracers return to their initial positions. In addition, to enforce the monotonicity of the advection process, the slope-limiter and FCT limiter are applied to the advection algorithms. In this way, the tracer distributions reflect the numerical properties of the advection algorithms.

The FFSL horizontal solver in combination with either the vertical PPM or RK3O3 algorithm allows monotonicity and generates nearly identical simulations, as shown in Fig. 7ab and Fig. 8ab. The overall shape and features of the tracer distribution are well preserved. The horizontal RK3O3 solver in combination with either the vertical PPM or RK3O3 algorithm causes some undershoots in the simulations. The undershoots are very small (0.099 and 0.098, the analytical value is 0.1), as shown in Fig. 7cd and Fig. 8cd. When comparing the maximum values of the four combinations, the slope-limiter with the FFSL has greater dissipation than the FCT limiter with RK3O3 does for the horizontal solver. The FCT limiter with RK3O3 has a larger degree of dissipation than the slope-limiter with PPM does for the vertical solver. However, these differences are not significant. If computational efficiency is a concern, a combination of the horizontal FFSL and vertical PPM is preferable.

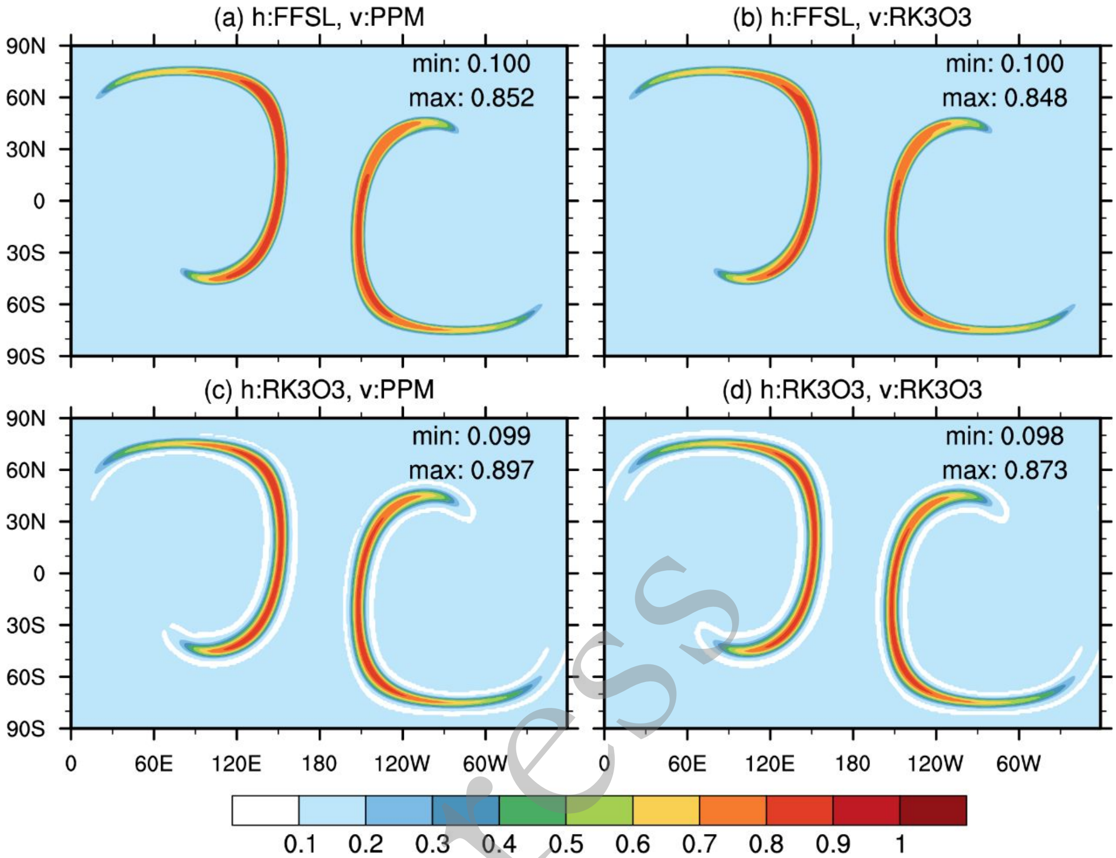

Fig. 7. The horizontal cross-sections of tracer q_3 at 4900 m on model day 6 of the DCMIP 1-1 three-dimensional deformational flow test. Two horizontal (FFSL and RK3O3) and two vertical (PPM and RK3O3) flux operators are used in the transport model. The resolution is 1° with 60 vertical levels. White areas show numerical undershoots. The minimum (min) and maximum (max) of each simulation are also shown in each panel.

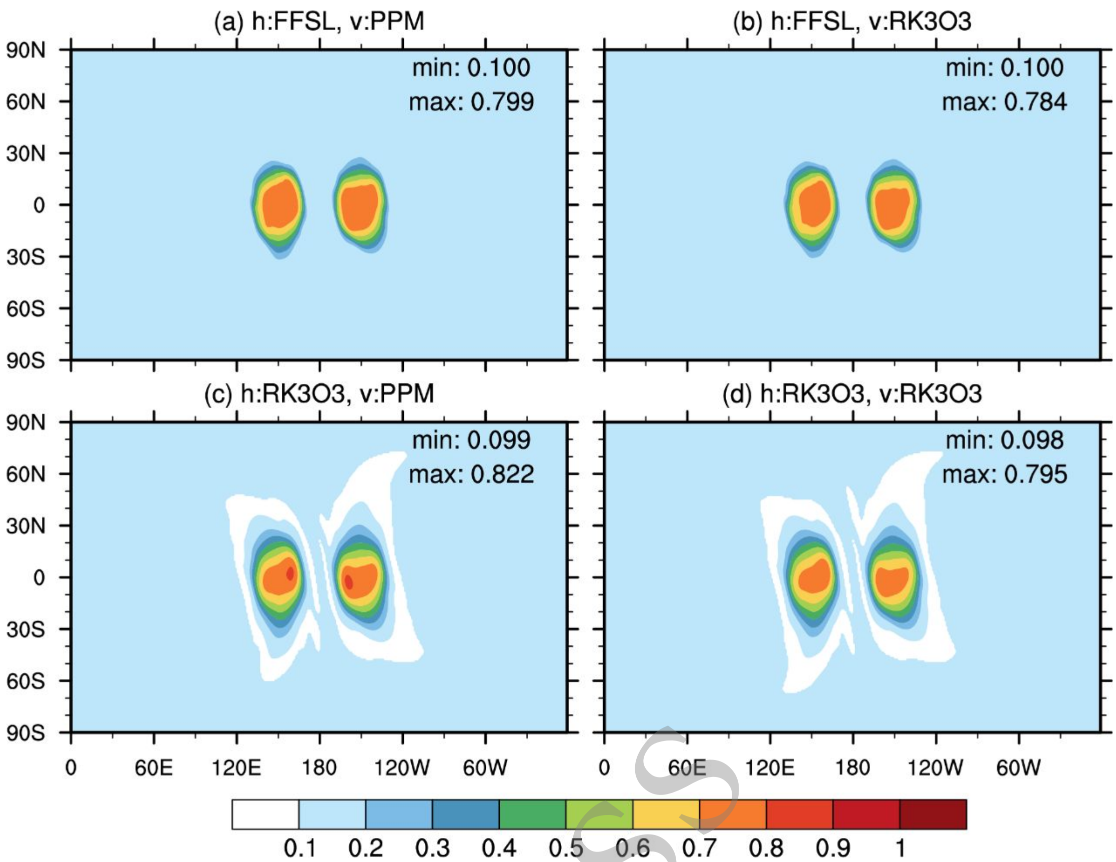

Fig. 8. Same as Fig. 7, but for T = 12 days.

In addition, this test can objectively evaluate the tracer model's ability to preserve the correlations between two tracer fields. The first tracer field (q_1) is specified as two cosine bells. The second tracer field (q_2) is nonlinearly correlated with the first tracer ($q_2 = 0.9 - 0.8 \cdot q_1^2$). We calculate the real mixing (ℓ_r), range-preserving unmixing (ℓ_u), and overshooting (ℓ_o) for q_1 and q_2, as described in Lauritzen and Thuburn (2012) and Kent et al. (2014).

The correlation plots and the mixing diagnostics, as shown in Fig. 9, demonstrate that there is no overshooting for the combination of the horizontal FFSL with the vertical PPM ($\ell_o = 0.0$). The other three configurations, however, exhibit slight overshoots. Moreover, this combination yields the smallest real mixing and unmixing values. The scatter plots also demonstrate that this combination best preserves the correlations.

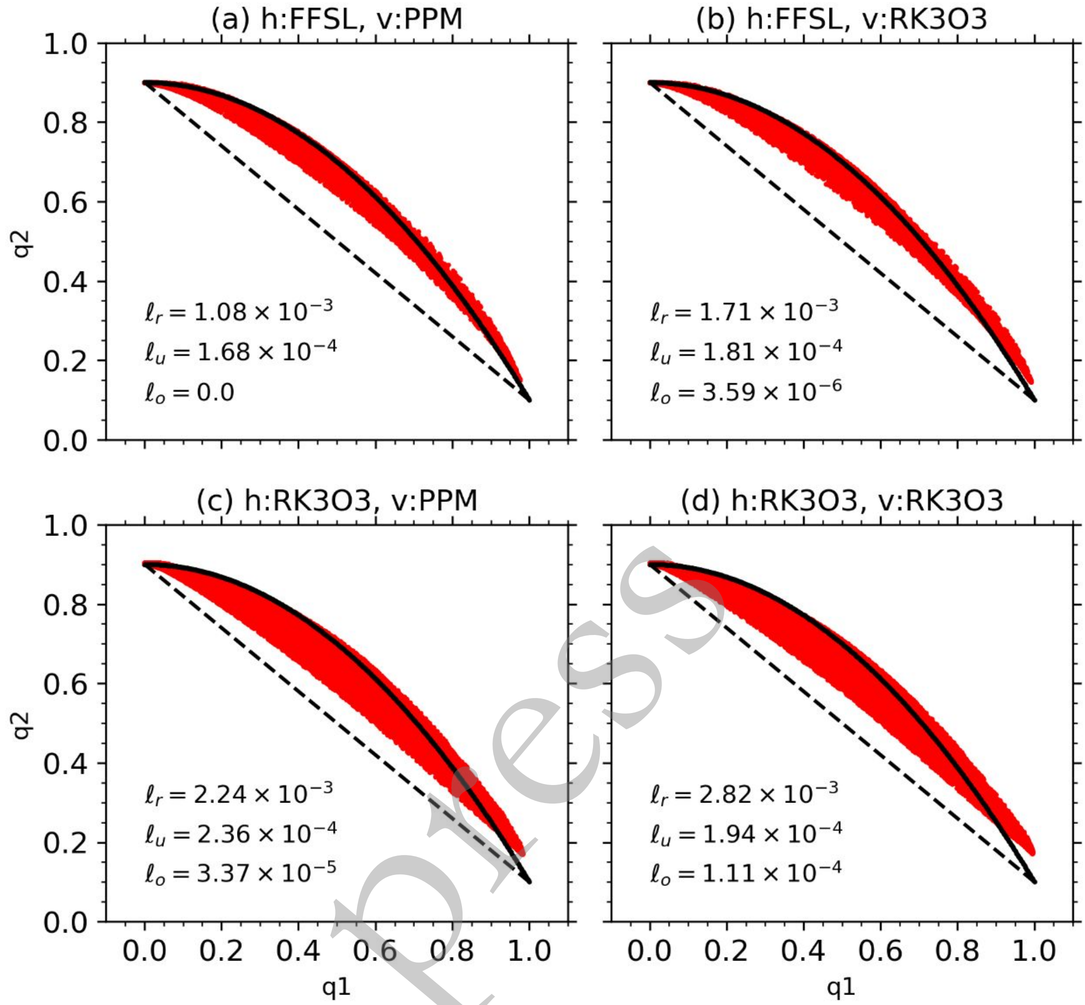

Fig. 9. Scatter plots of two nonlinearly correlated tracer fields, q_1 and q_2, in the five vertical levels around a height of 4900 m at $T = 6$ days. The mixing diagnostics ℓ_r, ℓ_u, and ℓ_o are calculated for each combination of two horizontal flux operators (FFSL and RK3O3) and two vertical flux operators (PPM and RK3O3).

3.4 Three-dimensional Hadley-like meridional circulation

The final experiment is Test Case 1 of the Kent et al. (2014) test suite. The deformational flow mimics the Hadley-like meridional circulation as prescribed in the experiment. The initial tracer field is a quasi-smooth cosine profile. Halfway through the simulation, the designed flow is reversed, and the tracers return to their initial shapes and positions, which provides an analytical solution at the end of the run. We can investigate the effect of the horizontal–vertical-splitting method on the accuracy of the scheme. Here, we first demonstrate that the adaptively implicit vertical advection algorithm can increase the time-step size in this case. The numerical convergence rates of several combinations of horizontal and vertical flux operators are then assessed.

Based on the analysis in the preceding subsection, the FFSL scheme and the PPM-based flux operator are used in the horizontal solver and the explicit part of the vertical solver, respectively. We keep the horizontal and vertical resolution constant while increasing the time-step size. The horizontal resolution is 1° with 180 vertical levels (1° L180). The time-step sizes are 120 s, 240 s, 360 s, and 450 s, respectively corresponding to maximum vertical Courant numbers of 0.59, 1.18, 1.76, and 2.21.

The vertical–meridional slices of the tracer field along the 180° longitude line at $t = 12$ hours and $t = 24$ hours are shown in Fig. 9 and Fig. 10 using the fully explicit and adaptively implicit schemes, respectively. The results of the fully implicit algorithm are also shown for reference. At $t = 12$ hours, the tracer field deforms to its maximum extent. At $t = 24$ hours, the tracer field closely resembles its initial phase, although there are some deviations or gaps near $30^{\circ}\mathrm{N/S}$, where the tracer field experiences the greatest stretch. The simulation results of the adaptively implicit and fully explicit algorithms are nearly identical, as expected, when the vertical Courant number falls within the stability limitation (i.e., 0.59 and 1.18). The diffusive property of the fully implicit algorithm is apparent, especially for the gapping at approximately $30^{\circ}N/S$. This is reasonable because the first-order upwind algorithm within the implicit scheme produces the diffusion. In the simulations using the fully explicit algorithm, as the vertical Courant number increases, some abnormal values arose and even caused the model to crash. However, neither the adaptively implicit nor fully implicit scheme produces any abnormal values, and the model remained stable with these two schemes. The former has much less diffusion than the latter at the same time levels. In other words, the adaptively implicit scheme diffuses selectively, whereas the fully implicit scheme yields diffusion almost everywhere. As a result, the adaptively implicit scheme can be implemented well in practical applications.

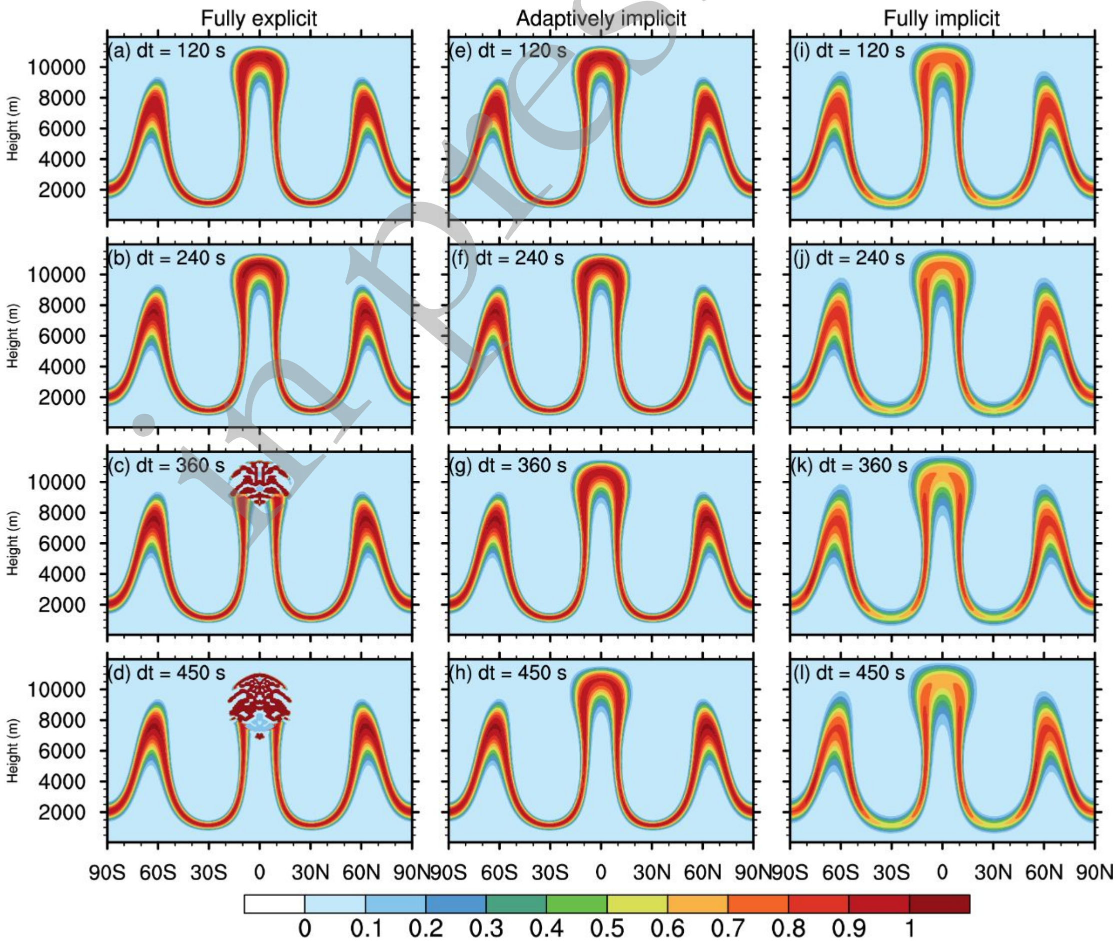

Fig. 10. The 3D Hadley-like meridional circulation test (DCMIP1-2): latitude–height

plot at the longitude of 180° at 12 h with four time-step sizes (from the upper rows to bottom rows: 120 s, 240 s, 360 s, 450 s) using fully explicit (left column, (a)-(d)), adaptively implicit (middle column, (e)-(h)), and fully implicit (right column, (i)-(l)) vertical advection schemes. There are 180 vertical levels with a horizontal resolution of 1°.

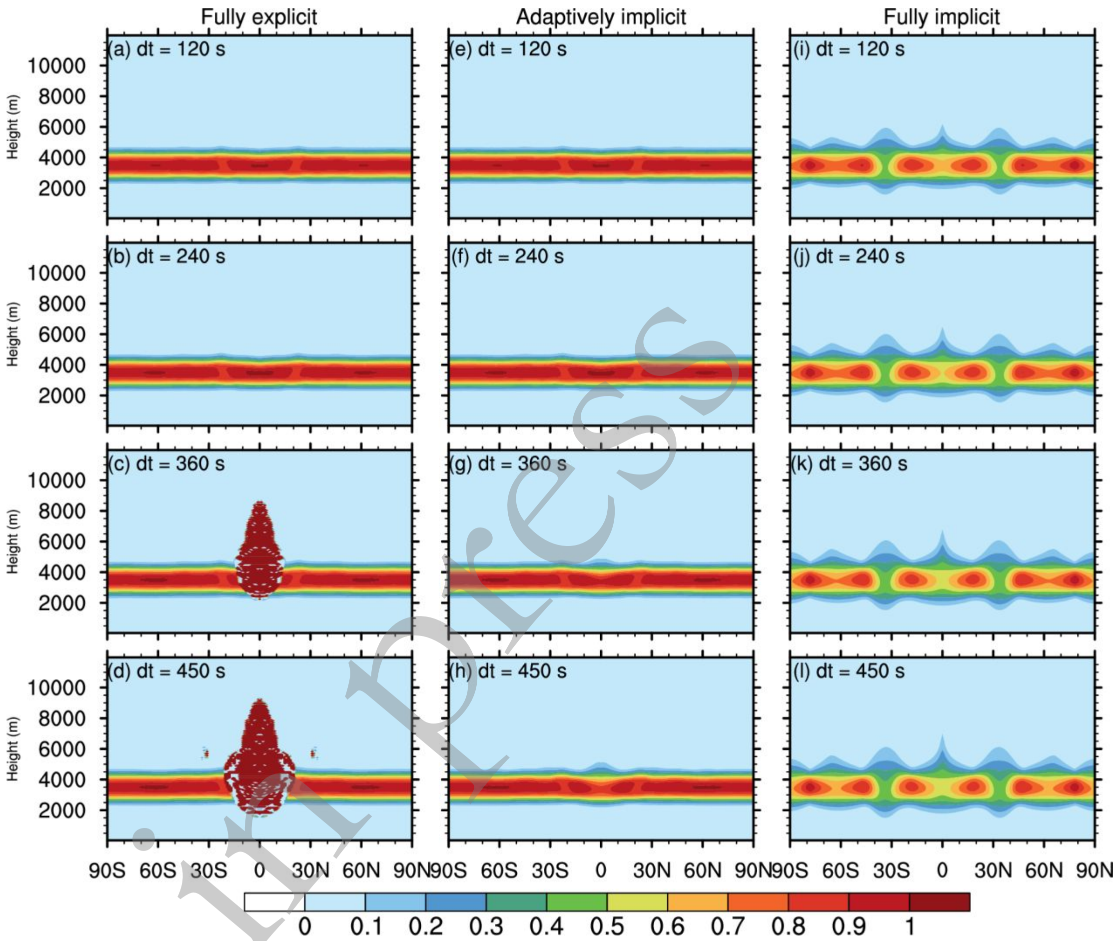

Fig. 11. Same as Fig. 10, but at 24 h.

To further assess the robustness of the adaptively implicit vertical algorithm, we calculate the convergence rates from the Hadley-like circulation test. The resolutions are set to 2°L90, 1°L180, and 0.5°L360 with time-step sizes of 720 s, 360 s, and 180 s, respectively, to trigger the adaptively implicit algorithm. The two horizontal flux operators and two vertical flux operators are combined to form four configurations. In addition, the monotonic slope-limiter is used in the PPM-based solvers, and the FCT flux limiter is also applied in each sub-step of the RK3 time integrator.

As seen in Fig. 12, all four combinations produce similar results in which the error norms converge between the first and second order, which is somewhat lower than those given in Kent et al. (2014). This is reasonable because the vertically implicit solver uses a first-order upwind algorithm. On the other hand, simple operator-splitting is used in the horizontal–vertical coupling. In addition, the numerical accuracy is also reduced by the non-uniform vertical spacings of the vertical coordinate. The RK3O3-based solvers exhibit marginally higher convergence rates than the PPM-based solvers do, and they are the same as the convergence rates in the two-dimensional solid-body rotation test (shown in Fig. 4). There are only minor differences among the four combinations in terms of $\ell_1, \ell_2, \ell_\infty$. In general, the PPM-based 3D solvers produce fewer errors than the RK3O3-based solvers do at each resolution, particularly for 2°L 90 and 1°L180. Overall, the outcomes are insensitive to the combination of two horizontal flux operators and two vertical flux operators, which further demonstrates the robustness of the 3D tracer transport model. These results are consistent with the results of the previous three-dimensional deformational flow test cases.

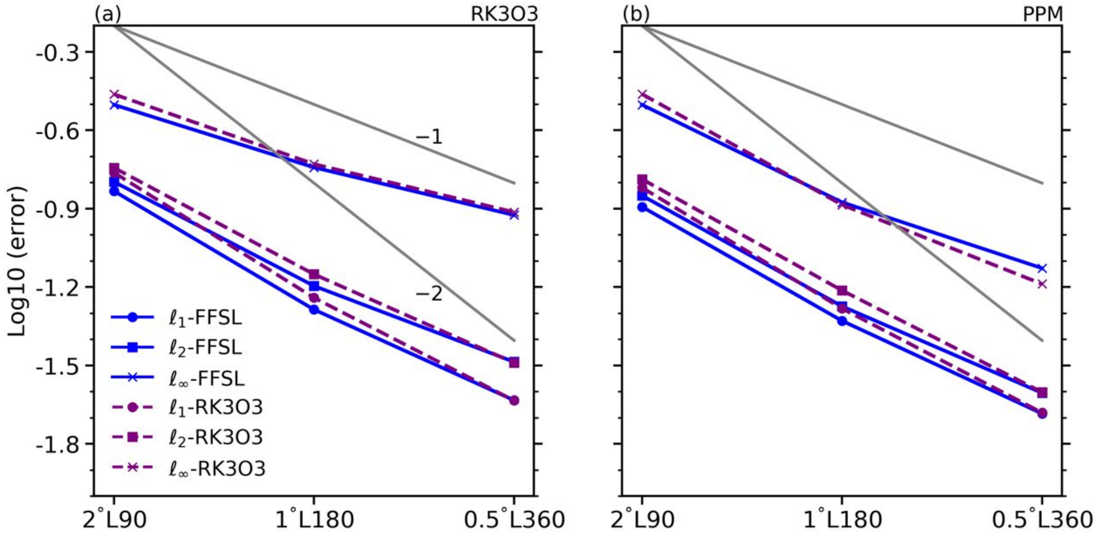

Fig. 12. The 3D Hadley-like meridional circulation test: numerical error norms of ℓ_1, ℓ_2, ℓ_∞ for the (a) PPM-based and (b) RK3O3-based vertically explicit transport solvers, with two horizontal transport schemes of FFSL and RK3O3. The gray lines denote the ideal first- and second-order convergence rates.

4. Conclusions

This study developed a three-dimensional tracer transport model on a regular latitude–longitude grid. The model maintains its computational stability in the presence of large Courant numbers. The model uses a flux-form conservation tracer equation, and the key is the flux computation on the mesh interface. To enable a high Courant number along the zonal direction within the scheme, a flux-form semi-Lagrangian (FFSL) scheme is chosen as the horizontal solver. An adaptively implicit vertical advection scheme is applied to enhance the stability of the vertical discretization. For comparison, we adopted a third-order upwind advection scheme with the third-order Runge–Kutta scheme (RK3O3) in the horizontal and vertical directions as a reference.

For the 2D test cases, the FFSL with slope-limiter is comparable to or better than the RK3O3 scheme with FCT in terms of accuracy and monotonicity. Furthermore, the FFSL allows for much larger time-step sizes than the RK3O3 does. The horizontal FFSL scheme in conjunction with the vertical PPM scheme is demonstrated to be the best configuration in terms of accuracy, monotonicity, and computational efficiency in the 3D advection tests. The stringent Courant number constraint can be alleviated via the adaptively implicit vertical advection algorithm, allowing the time-step size to be increased.

The 3D tracer transport model has been implemented in the global atmospheric baroclinic dynamical core we are developing, and only the tracer transport module was evaluated in this work. Further work on the coupling of the tracer transport module and the dynamical core with one or two physics packages may be available in the near future. Additionally, the use of the incremental remapping method and the floating Lagrangian vertical coordinate presents promising alternatives that are not constrained by the vertical Courant number. Further exploration can be pursued in these areas for future research.

Acknowledgments This work was jointly supported by the National Natural Science Foundation of China (NSFC; 42075153) and the Young Scientists Fund of Earth System Modeling and Prediction Centre (CEMC-QNJJ-2022014).

Data availability Data for this study are available from the first author upon request.

Appendix A.

A minor error in the monotonicity constraints for the PPM in Lin (2004)

In order to ensure monotonicity, a slope limiter is required in the FFSL transport scheme. Constraining the slope or mismatch is a critical process. In Appendix B of Lin (2004), there is a minor error in equation (B1) for constraining the mismatch. The correct formulation is:

$$\Delta q_i^{mono} = sign\left[\min\left(|\Delta q|, \Delta q_i^{min}, \Delta q_i^{max}\right), \Delta q_i\right] \tag{A1}$$

instead of:

$$\Delta q_i^{mono} = sign\left[\min\left(\left|\Delta q_i^{min}\right|, \Delta q_i^{min}, \Delta q_i^{max}\right), \Delta q_i\right]. \tag{A2}$$

Where Δq_i is the “mismatch” that represents the difference between $q_{i+1/2}$ and $q_{i-1/2}$ for the ith cell. The superscript “mono” denotes the final value used for monotonicity. The superscripts of “min”, “max” denote the values needed in the calculation, and same as in Lin (2004). The functions sign, min, and max are as defined in the Fortran language as in Lin (2004).

REFERENCES

Arakawa, A., and V. R. Lamb, 1977: Computational Design of the Basic Dynamical Processes of the UCLA General Circulation Model. *General Circulation Models of the Atmosphere*, J. CHANG, Ed., Vol. 17 of *Methods in Computational Physics: Advances in Research and Applications*, Elsevier, 173–265

Book, D. L., Boris, J. P., and Zalesak, S. T., 1981: Flux-corrected transport. In D. L. Book (Ed.), Finite-difference techniques for vectorized fluid dynamics calculations, Springer Series in Computational Physics (pp. 29–55). Berlin, Heidelberg: Springer.

Boris, J. P., Book, D. L., 1997: Flux-corrected transport. *J. Comput. Phys*, **135**(2), 172–186.

Carpenter, R. L., K. K. Droegemeier, P. R. Woodward, and C. E. Hane, 1990: Application of the Piecewise Parabolic Method (PPM) to Meteorological Modeling. *Mon. Weather Rev.*, **118**, 586–612.

Chen, Y., H. Weller, S. Pring, and J. Shaw, 2017: Comparison of dimensionally split and multi-dimensional atmospheric transport schemes for long time steps. *Q. J. R. Meteorol. Soc*, **143**: 2764-2779.

Colella, P., and P. R. Woodward, 1984: The Piecewise Parabolic Method (PPM) for gas-dynamical simulations. *J. Comput. Phys.*, **54**, 174–201.

Diamantakis, M., 2014: The semi-Lagrangian technique in atmospheric modelling: current status and future challenges. Seminar on Recent Developments in Numerical Methods for Atmosphere and Ocean Modelling, 2-5 September 2013, Shinfield Park, Reading, ECMWF, https://www.ecmwf.int/node/9054.

Durran, D. R., 2010: *Numerical Methods for Fluid Dynamics: With Applications to Geophysics*, 1689–1699.

Godunov, S. K., 1959: A Finite Difference Method for the Numerical Computation of Discontinuous Solutions of the Equations of Fluid Dynamics. *Matematicheskii Sbornik*, 47, 271–306.

Hall, D. M., P. A. Ullrich, K. A. Reed, C. Jablonowski, R. D. Nair, and H. M. Tufo, 2016: Dynamical Core Model Intercomparison Project (DCMIP) tracer transport test results for CAM-SE. *Q. J. R. Meteorol. Soc.*, **142**, 1672–1684, https://doi.org/10.1002/qj.2761.

Hundsdorfer, W., Verwer, J. G., 2003: Numerical Solution of Time-Dependent Advection–Diffusion–Reaction Equations. Springer Series in Computational Mathematics. Springer, New York

Hyman, J.M., 1979: A method of lines approach to the numerical solution of conservation laws. In: Vichnevetsky, R., Stepleman, R.S. (Eds.), Advances in Computer Methods for Partial Differential Equations, vol. III, pp. 313–321, (Pub. IMACS)

Jablonowski, C., M. Herzog, J. E. Penner, R. C. Oehmke, Q. F. Stout, B. van Leer, and K. G. Powell, 2006: Block-Structured Adaptive Grids on the Sphere: Advection Experiments. *Mon. Weather Rev.*, **134**, 3691–3713.

Kasahara, A., 1974: Various Vertical Coordinate Systems Used for Numerical Weather Prediction. *Mon. Weather Rev.*, **102**, 509–522.

Kent, J., C. Jablonowski, J. P. Whitehead, and R. B. Rood, 2012: Assessing Tracer Transport Algorithms and the Impact of Vertical Resolution in a Finite-Volume Dynamical Core. *Mon. Weather Rev.*, **140**, 1620–1638.

Kent, J., P. A. Ullrich, and C. Jablonowski, 2014: Dynamical core model intercomparison project: Tracer transport test cases. *Q. J. R. Meteorol. Soc.*, **140**, 1279–1293.

Laprise, R., 1992: The Euler Equations of Motion with Hydrostatic Pressure as an Independent Variable. *Mon. Weather Rev.*, **120**, 197–207.

Lauritzen, P. H., and J. Thuburn, 2012: Evaluating advection/transport schemes using interrelated tracers, scatter plots and numerical mixing diagnostics. *Q. J. R. Meteorol. Soc.*, **138**, 906–918, https://doi.org/10.1002/qj.986.

Lauritzen, P. H., P. A. Ullrich, R. D. Nair, 2011: Atmospheric Transport Schemes: Desirable Properties and a Semi-Lagrangian View on Finite-Volume Discretizations. In: Lauritzen, P., Jablonowski, C., Taylor, M., Nair, R. (eds) Numerical Techniques for Global Atmospheric Models. Lecture Notes in Computational Science and Engineering, vol 80. Springer, Berlin, Heidelberg. https://doi.org/10.1007/978-3-642-11640-7_8

Leveque, R. J., 2004: *Finite-Volume Methods for Hyperbolic Problems*. Cambridge university press.

Li, J., B. Wang, and L. Dong, 2020: Analysis of and Solution to the Polar Numerical Noise Within the Shallow-Water Model on the Latitude-Longitude Grid. *J. Adv. Model. Earth Syst.*, **12**, e2020MS002047, https://doi.org/10.1029/2020MS002047.

Li, J., and Y. Zhang, 2022: Enhancing the stability of a global model by using an adaptively implicit vertical moist transport scheme. *Meteorol. Atmos. Phys.*, **134**, 55.

Lin, S.-J., and R. B. Rood, 1996: Multidimensional Flux-Form Semi-Lagrangian Transport Schemes. *Mon. Weather Rev.*, **124**, 2046–2070.

Lin, S.-J., and R. B. Rood, 1997: An explicit flux-form semi-lagrangian shallow-water model on the sphere. *Q. J. R. Meteorol. Soc.*, **123**, 2477–2498.

Lin, S.-J., 2004: A "Vertically Lagrangian" Finite-Volume Dynamical Core for Global Models. *Mon. Weather Rev.*, **132**, 2293–2307.

Nair, R. D., and C. Jablonowski, 2008: Moving Vortices on the Sphere: A Test Case for Horizontal Advection Problems. *Mon. Weather Rev.*, **136**, 699–711.

Nair, R. D., and B. Machenhauer, 2002: The Mass-Conservative Cell-Integrated Semi-Lagrangian Advection Scheme on the Sphere. *Mon. Weather Rev.*, **130**, 649–667.

Nair, R. D., and P. H. Lauritzen, 2010: A class of deformational flow test cases for linear transport problems on the sphere. *J. Comput. Phys.*, **229**, 8868–8887.

Norman, M. R., and R. D. Nair, 2018: A Positive-Definite, WENO-Limited, High-Order Finite Volume Solver for 2-D Transport on the Cubed Sphere Using an ADER Time Discretization. *J. Adv. Model. Earth Syst.*, **10**, 1587–1612, https://doi.org/10.1029/2017MS001247.

Putman, W. M., and S.-J. Lin, 2007: Finite-volume transport on various cubed-sphere grids. *J. Comput. Phys.*, **227**, 55–78.

Satoh, M., B. Stevens, F. Judt, M. Khairoutdinov, S.-J. Lin, W. M. Putman, and P. Düben, 2019: Global Cloud-Resolving Models. *Curr. Clim. Chang. Reports*. **5**, 172–184.

Shchepetkin, A. F., 2015: An adaptive, Courant-number-dependent implicit scheme for vertical advection in oceanic modeling. *Ocean Model.*, **91**, 38–69.

Simmons, A. J., and D. M. Burridge, 1981: An Energy and Angular-Momentum Conserving Vertical Finite-Difference Scheme and Hybrid Vertical Coordinates. *Mon. Weather Rev.*, **109**, 758–766.

Skamarock, W. C., and A. Gassmann, 2011: Conservative Transport Schemes for Spherical Geodesic Grids: High-Order Flux Operators for ODE-Based Time Integration. *Mon. Weather Rev.*, **139**, 2962–2975.

Staniforth, A., and J. Côté, 1991: Semi-Lagrangian Integration Schemes for Atmospheric Models—A Review. *Mon. Weather Rev.*, **119**, 2206–2223, https://doi.org/10.1175/1520-0493(1991)119<2206:SLISFA>2.0.CO;2.

Stevens, B., and Coauthors, 2019: DYAMOND: the DYnamics of the Atmospheric general circulation Modeled On Non-hydrostatic Domains. *Prog. Earth Planet. Sci.*, **6**, 61.

Strang, G., 1968: On the construction and composition of difference schemes. *SIAM J. Numer. Anal.*, **5**, 506–517.

Weller, H., 2012: Controlling the Computational Modes of the Arbitrarily Structured C Grid. *Mon. Weather Rev.*, **140**, 3220–3234, https://doi.org/10.1175/MWR-D-11-00221.1.

Weller, H., J. Woodfield, C. Kühnlein, and P. K. Smolarkiewicz, 2022: Adaptively implicit MPDATA advection for arbitrary Courant numbers and meshes. *Q. J. R. Meteorol. Soc.*, 1–20, https://doi.org/10.1002/qj.4411.

Wicker, L. J., and W. C. Skamarock, 2002: Time-Splitting Methods for Elastic Models Using Forward Time Schemes. *Mon. Weather Rev.*, **130**, 2088–2097.

Wicker, L. J., and W. C. Skamarock, 2020: An Implicit–Explicit Vertical Transport Scheme for Convection-Allowing Models. *Mon. Weather Rev.*, **148**, 3893–3910.

Williamson, D. L., 2007: The Evolution of Dynamical Cores for Global Atmospheric Models. *J. Meteorol. Soc. Japan. Ser. II*, **85B**, 241–269.

Williamson, D., L., J. B. Drake, J. J. Hack, R. Jakob, and P. N. Swarztrauber, 1992: A standard test set for numerical approximations to the shallow water equations in spherical geometry. *J. Comput. Phys.*, **102**, 211–224.

Wood, N., A. Staniforth, A. White, T. Allen, M. Diamantakis, M. Gross, T. Melvin, C. Smith, S. Vosper, M. Zerroukat, and J. Thuburn, 2014: An inherently mass-conserving semi-implicit semi-Lagrangian discretization of the deep-atmosphere global non-hydrostatic equations. *Q. J. R. Meteorol. Soc.*, **140**, 1505–1520, https://doi.org/10.1002/qj.2235.

Zalesak, S. T. 1979: Fully multidimensional flux-corrected transport algorithms for fluids. *J. Comput. Phys.*, **31**(3), 335–362.

Zhang, Y., J. Li, R. Yu, Z. Liu, Y. Zhou, X. Li, and X. Huang, 2020: A Multiscale Dynamical Model in a Dry-Mass Coordinate for Weather and Climate Modeling: Moist Dynamics and Its Coupling to Physics. *Mon. Weather Rev.*, **148**, 2671–2699, https://doi.org/10.1175/MWR-D-19-0305.1.